

Article

# A Numerical Model for the Scour Effect on the Bearing Capacity of an Offshore Wind Turbine with a Five-Bucket Jacket Foundation

Hang Zhu <sup>1,2</sup> , Jijian Lian <sup>1,2,3,\*</sup>, Yaohua Guo <sup>1,2</sup>  and Haijun Wang <sup>1,2</sup>

<sup>1</sup> State Key Laboratory of Hydraulic Engineering Intelligent Construction and Operation, Tianjin University, Tianjin 300072, China; zhuhang@tju.edu.cn (H.Z.)

<sup>2</sup> School of Civil Engineering, Tianjin University, Tianjin 300072, China

<sup>3</sup> School of Computer Science and Engineering, Tianjin University of Technology, Tianjin 300384, China

\* Correspondence: jjlian@tju.edu.cn

**Abstract:** As offshore wind farms move into deeper waters and the capacity of offshore wind turbines (OWTs) increases, a new type of OWT foundation needs to be developed. In this study, a new type of five-bucket jacket foundation (FBJF) was proposed based on the broad application of a multi-bucket jacket foundation (MBJF) in offshore wind farms. The soil around the OWT foundation is subject to scour due to the complex marine environment. To investigate the effects of scouring on the FBJF, a series of local-scour simplified finite-element models of the FBJF were established using ABAQUS, and the effects of scouring depth and the extent on the bearing capacity of the FBJF with the monotonic load were analyzed. Then, the failure envelopes of the FBJF under combined loading were obtained using the fixed-displacement ratio method, and the effects of various scour conditions on the failure envelopes were compared. The results indicate that the failure envelope profile contracts inward, and the bearing capacity decreases with the increasing scouring depth and extent. Furthermore, the failure envelopes of the FBJF under different vertical loads were calculated, and the  $F_V$ - $F_H$ - $F_M$  failure envelopes of the FBJF were obtained through interpolation. Finally, the effects of different scour conditions on the  $F_V$ - $F_H$ - $F_M$  failure envelopes of the FBJF were analyzed. The results show that the  $F_V$ - $F_H$ - $F_M$  failure envelopes of the FBJF have similar profiles and follow the same trend under different scour conditions.



**Citation:** Zhu, H.; Lian, J.; Guo, Y.; Wang, H. A Numerical Model for the Scour Effect on the Bearing Capacity of an Offshore Wind Turbine with a Five-Bucket Jacket Foundation. *J. Mar. Sci. Eng.* **2024**, *12*, 753. <https://doi.org/10.3390/jmse12050753>

Received: 1 April 2024  
Revised: 28 April 2024  
Accepted: 29 April 2024  
Published: 30 April 2024



**Copyright:** © 2024 by the authors. Licensee MDPI, Basel, Switzerland. This article is an open access article distributed under the terms and conditions of the Creative Commons Attribution (CC BY) license (<https://creativecommons.org/licenses/by/4.0/>).

**Keywords:** bearing capacity; offshore wind turbine; scouring; bucket foundation

## 1. Introduction

Wind energy is widely used to effectively reduce the dependence on non-renewable energy sources and global carbon emissions. Compared to onshore wind power, offshore wind energy is abundant and has broad development prospects due to its higher wind speed and lower wind pressure [1–3]. As offshore wind power develops, the unit capacity of OWTs is increasing. Additionally, with nearshore wind farm saturation, offshore wind power is trending towards deep-sea and large-capacity OWTs [4,5]. Currently, there are mainly two installation methods for OWT foundations: modular installation and integrated installation. Depending on the type of OWT foundation, different installation technologies are required. The integrated installation technology for offshore wind turbines is more innovative and able to effectively reduce construction costs and periods [6,7].

The construction cost of OWT foundations accounts for about 30% of the total investment in offshore wind power and rises with the water depth [8]. Therefore, it is crucial to select a proper foundation based on the marine environment and geological conditions of the installation site to reduce the cost and increase the efficiency of the OWT project. Figure 1 shows commonly used foundations for various water depths and geological situations,

including gravity foundations, monopile foundations, wide-shallow bucket foundations (WSBFs), multi-bucket jacket foundations (MBJFs), and floating foundations [9–14].

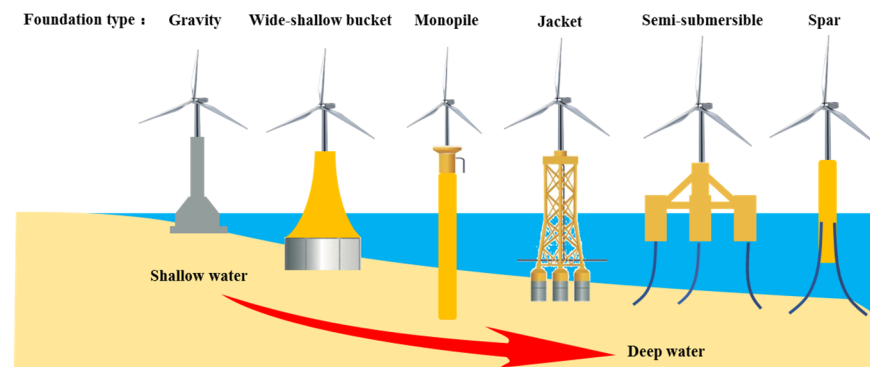


**Figure 1.** Foundation types for OWTs.

Compared with other types, bucket foundations offer the superiorities of low construction cost and a short construction period [15]. In addition, jacket structures are suitable for deep water because their spatial truss structure provides high rigidity and reduces wave and current loads [16–18]. Therefore, the MBJF combines the advantages of a suction bucket foundation and a jacket structure, which is suitable for the deep sea and convenient for construction.

The MBJF was initially used on the Draupner E platform and the Sleipner T platform [19,20]. Subsequently, SPT Offshore was the first to apply the MBJF in offshore wind power. As shown in Figure 2, tripod bucket jacket foundations were successfully installed in the Borkum Riffgrund offshore wind farm in Germany and the Aberdeen offshore wind farm in the UK [21–23]. In China, four-bucket jacket foundations and tripod bucket jacket foundations were also successfully installed at the Zhuanghe and Changle offshore wind farms, respectively. The successful implementation of the above practical projects reflects the extensive application of the MBJF in offshore wind power.

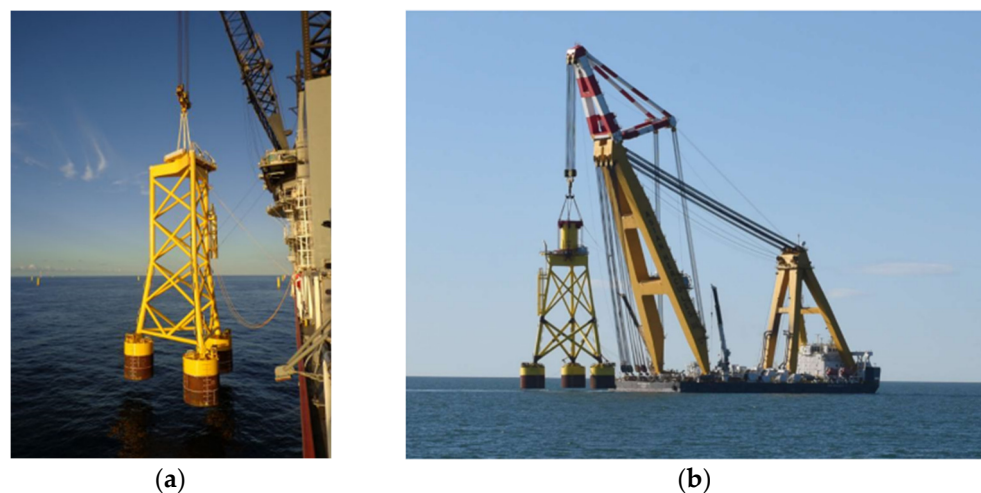


**Figure 2.** MBJF actual projects: (a) Borkum Riffgrund; (b) Aberdeen.

As a kind of fixed foundation for OWTs, the MBJF not only suffers the vertical load brought by its weight during normal operation but also withstands horizontal loads and bending loads brought by wind and waves. All these loads are transmitted to the soil through the lower bucket foundations. Therefore, it is meaningful to investigate the bearing capacity of the foundation under combined loading and the interaction between the foundation with the surrounding soil [24]. The failure envelope is critical for evaluating

the bearing capacity of a fixed foundation, which is a limit for the overall failure of the soil under combined loading, and the foundation can be considered safe within this limit [25]. Many scholars have used the failure envelope to study the bearing capacity characteristics of bucket foundations under combined loading. Ding et al. [26] verified the numerical model for calculating the bearing capacity of the WSBF in clay through experiments, clarified the soil failure modes and mechanisms of the WSBF under horizontal loads, and provided an analytical expression for the ultimate bearing capacity. In addition, the failure envelope of the WSBF under combined loading was also investigated with the help of the finite-element method.

Liu et al. [27] analyzed the  $H_{ult}$  of the WSBF in homogeneous saturated sand using experimental and finite-element methods and compared the  $H_{ult}$  of the WSBF with various height/diameter ratios and the differences in soil failure modes. The results showed that the failure mode of the WSBF is rotational, and the rotation center is related to the height/diameter ratio of the foundation under horizontal loading. Jia et al. [28] investigated the  $H_{ult}$  of the WSBF in saturated silty sand through field experiments and clarified that when the elastic modulus of the sand in the finite-element model is 4–5 times that of the experiment sand, the load–displacement curves of the two can match well. Wang et al. [29] addressed the issue of asymmetric failure envelopes of the WSBF under combined loading. By moving the load application point to the rotation center, optimized failure envelopes were obtained. An algebraic equation was established for the failure envelope, which had simple parameters and could be applied to actual projects. Yin. [30] analyzed the effects of factors such as soil strength and embedment depth ratio on the failure envelope of skirted spudcan foundations in soft clay through a series of finite-element model calculations. The results showed that the size of the failure envelope is significantly affected, while the shape of the failure envelope is less affected by factors.

Compared to the WSBF, the MBJF is subject to more factors affecting its bearing capacity and has a different failure mode. Gourvenec et al. [31,32] studied the effects of bucket spacing and embedment on the failure modes of a rigidly connected two-footing foundation and calculated the failure envelopes by using the finite-element method. Moreover, it was compared with a single bucket of the equivalent bearing area and embedment. Kim et al. [33,34] calculated the vertical bearing capacity, horizontal bearing capacity, and bending bearing capacity of tripod bucket foundations in undrained clay by the finite-element method, considering factors such as bucket spacing and embedded depth. The results were compared with a single bucket foundation to obtain the corresponding group efficiency factors. In addition, the failure envelopes of the MBJF under combined horizontal and bending loads were investigated, considering factors such as the non-homogeneity of clay and  $F_V$ , and then the design equations of the envelope were established. Tran et al. [35] studied the horizontal and bending capacities of tripod bucket foundations in the sand using the numerical method, considering factors such as bucket spacing, bucket diameter, and bucket height. The results showed that the horizontal bearing capacity reached a maximum at a certain specific bucket spacing and height, while the bending bearing capacity continuously improved with increasing bucket spacing.

The previous studies on the bearing capacity characteristics of the foundations are ideal without considering the scouring of the soil around the foundation. However, for fixed OWT foundations like bucket foundations, the flow field around the foundation is complex due to the influences of waves and currents, making the seabed soil susceptible to scouring [36]. Scouring can lead to a decrease in bearing capacity, which can threaten the response and stability of the overall structure of offshore wind power. Therefore, the prediction and prevention of scouring have also garnered attention from related scholars [37]. Kishore et al. [38] conducted experiments on two different stiffness monopile foundations in soft clay with and without scouring under different eccentric lateral loading conditions. The results indicated that scouring reduced the lateral bearing capacity of the foundation. Ni et al. [39] studied the effects of scouring on the bearing capacity of pile foundations in

the sand using numerical simulation and considered the soil stiffness and pile slenderness ratio. The results showed that scouring affected the shorter pile foundations significantly.

Some scholars established simplified numerical models of the local scour for the WSBF and four-bucket jacket foundation to study the effects of different scour conditions on the bearing capacity and failure envelopes of the foundations [40,41]. These studies indicate that scouring can lead to a reduction in the bearing capacity of the foundations and even threaten the safety of the foundations. Therefore, for the FBJF proposed in this study, it is meaningful to investigate the effects of scouring on the bearing capacity of the FBJF under monotonic loading and quantify the bearing capacity-reduction factors. In addition, investigating the failure envelope of the FBJF can provide a reference for the calculation of the bearing capacity of the FBJF after scouring.

In this study, a novel FBJF is proposed based on the trends of deep-sea and large-capacity OWT foundations. Then, the effects of scouring depth and extent on the ultimate bearing capacity of the FBJF are analyzed and quantified by a series of local-scour simplified finite-element models of the FBJF. Furthermore, the failure envelopes of the FBJF and the effects of various scour conditions are researched using the fixed-displacement ratio method. In addition, the failure envelopes of the FBJF under different vertical loads are calculated, and the  $F_V$ - $F_H$ - $F_M$  failure envelopes are investigated using the interpolation method. Finally, the effects of different scour conditions on the  $F_V$ - $F_H$ - $F_M$  failure envelope are discussed.

## 2. Concept Development

The FBJF (Figure 3) mainly consists of the upper jacket, the middle composite beam system, and the lower five-bucket foundation. The middle of the upper jacket is supported by an X-shaped brace, with a transition section at the top connecting to the tower. The middle composite beam system is composed of section steel, which not only prevents stress concentration but also enhances the stiffness of the top cover of the bucket, effectively avoiding sudden changes in suction pressure when the foundation floats or sinks into the soil. The lower five-bucket foundation consists of five bottom-open buckets, essentially adding an irregular bucket in the middle of the four-bucket foundation.

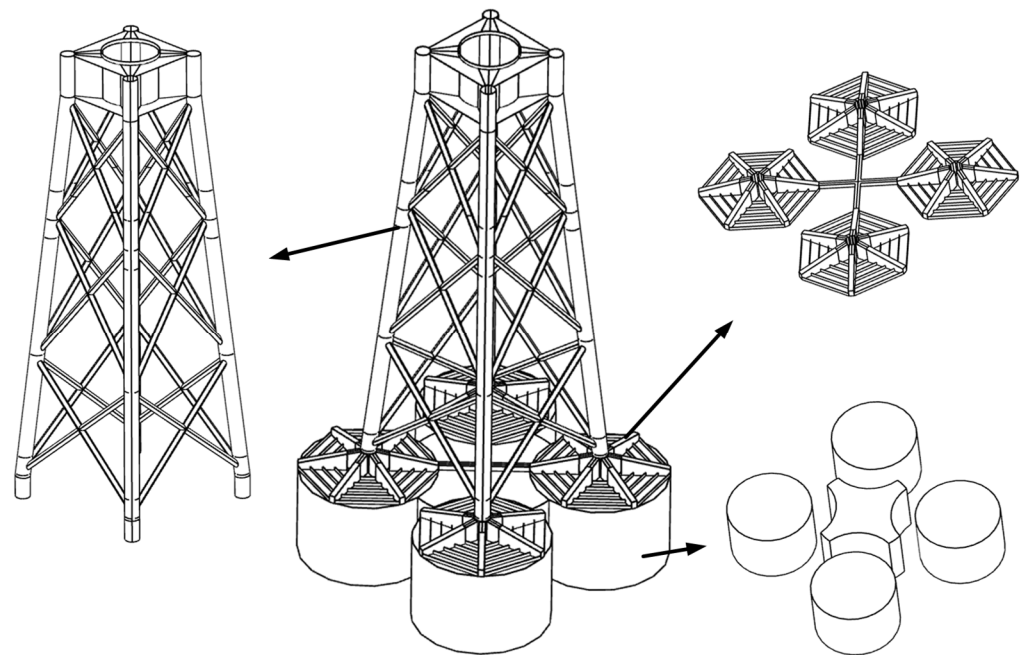


**Figure 3.** Schematic representation of the FBJF.

The novel design of the FBJF offers two main advantages. Firstly, compared to the WSBF, the buckling resistance of each bucket is superior to that of large-diameter bucket foundations. Additionally, the upper part of the foundation is a jacket structure with a

small flow resistance area, which can effectively reduce wave and current loads. For the same amount of steel and loads, the mudline inclination of the FBJF is less than that of the WSBF. When the mudline inclination rate and loads are the same, the amount of steel used for the FBJF is less than that of the WSBF, which makes the FBJF more economical. In addition, since the underwater transition section of the WSBF has a large water-blocking area and is subject to large wave loads, it is not suitable for deep water. However, the FBJF, with the lower bucket and the upper jacket, can be applied in deep-sea areas and meet the bearing capacity requirements. Specifically, the FBJF can be applied to a water depth of 45 m and subjected to environmental loads with a maximum wave height of 21 m and a current speed of 1.2 m/s. Secondly, compared to the MBJF, the FBJF includes an additional central bucket, which reduces the mudline inclination rate of the foundation under the same loads and provides additional buoyancy. This allows for the integrated transportation and one-step installation of the FBJF with transport ships, as shown in Figure 4.



**Figure 4.** Integrated transportation concept of the FBJF.

### 3. Failure Models of the FBJF under Monotonic Loading

#### 3.1. Finite-Element Model and Verification

Model experiments were conducted to verify the numerical simulation method of computing the bearing capacity of the FBJF, as shown in Figure 5. The model consists of an upper jacket, a middle composite beam system, and a five-bucket foundation at the bottom with a geometric similarity ratio of 1:100. The total height of the jacket is 650 mm, and the bottom five-bucket foundation consists of a central irregular bucket and four surrounding buckets, all with a skirt height of 120 mm. The diameter of the central irregular bucket is 260 mm, while the diameter of the surrounding buckets is 180 mm, with a center-to-center distance of 210 mm between adjacent buckets.

The same maintenance was carried out on the soil before each experiment to ensure that the soil properties were the same for each experiment. The FBJF model was placed at the center of the experimental box, and the hydraulic loading device was installed on the wall reaction beam, with the point of action of the loading device at the top of the jacket. A pressure sensor of type Weekend DSC-B2-5T, sourced from Tianjin, China, with a range of 200 kg and an accuracy of 0.05% FS, was located between the top of the jacket and the hydraulic rod to measure the horizontal load on the FBJF during the loading process. A laser displacement sensor of type Panasonic HG-C1400, sourced from Suzhou, China, with a range of 400 mm and an accuracy of 0.3 mm, was installed on the loading device to measure the horizontal displacement of the FBJF during the loading process.

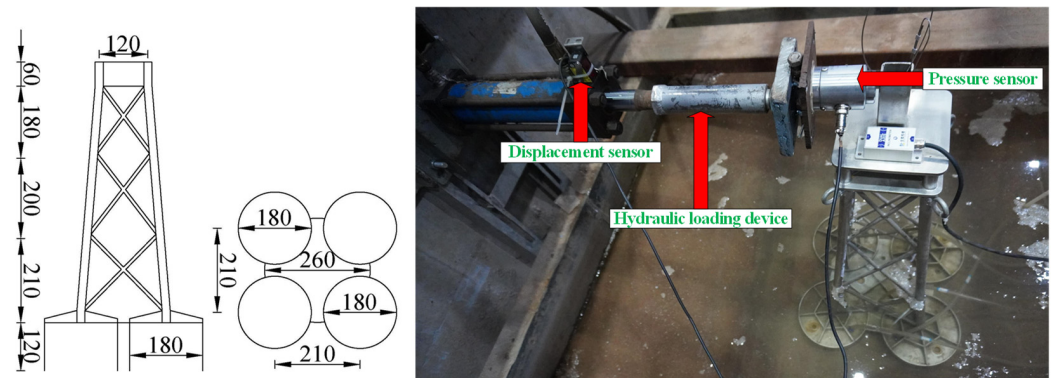


**Figure 5.** The experimental model and equipment of the FBjf (unit: mm).

Based on the experimental results, numerical simulations are conducted using ABAQUS 6.11 finite-element software. The FBjf model is established with the same dimensions as the experiment and uses identical parameters for the soil. The calculated results at the same loading positions are compared with the experimental results. If there is a significant difference between the two results, adjustments to the soil parameter values in the finite-element model must be made, followed by a rerun of the calculation. If the experimental results match well with the numerical simulation results, the finalized parameters for the finite-element model are as follows: the foundation is simulated using shell elements (S4R), assigned as rigid bodies with material properties of the Q345 steel. The soil is simulated by applying the Mohr-Coulomb model using solid elements (C3D8R), and the density is  $920 \text{ kg/m}^3$ , Young's modulus is 19.71 MPa, cohesion is 3 kPa, Poisson's ratio is 0.25, and the internal friction angle is  $31.4^\circ$ . The contact between the foundation and the soil is frictional contact with a friction coefficient of 0.25, which allows the separation. A full constraint is set at the base of the soil, while horizontal constraints are set around the soil.

The ultimate bearing capacities can be determined using the tangential intersection method based on load–displacement curves [42,43]. The intersection point of the two tangents is taken as the location where the failure of the FBjf occurs, the corresponding load is the ultimate bearing capacity, and the displacement relating to the ultimate load is the ultimate displacement of the FBjf. Figure 6 illustrates the load–displacement curves for experiments and numerical simulations under two different loading directions ( $0^\circ$  and  $45^\circ$ ). Horizontal load gradually increases with displacement until it stabilizes or changes slowly. In the two loading directions, the horizontal load capacity is almost the same. The  $H_{ult}$  results of the experiment and the numerical simulation match well with 213 N ( $H_0$ ) and 229 N ( $H_1$ ), respectively, with a difference of 7.5%. The comparison between the experimental and numerical results of the horizontal bearing capacity indicates the suitability of the numerical simulation methodology for studying the bearing capacity of the FBjf in subsequent calculations. Many scholars have validated their finite-element models using similar methods [40,44].

For the impacts of scouring on the bearing capacity of the FBjf, the effects of both the scouring extent and depth of the scour pit are considered separately. Figure 7 shows the schematic diagram of the scour pit of the FBjf, where  $S_{tw}$  is the scouring extent of the top of the scour pit,  $S_w$  is the scouring extent of the bottom of the scour pit, and  $S_d$  is the depth of the scour pit. In the numerical simulation process, it is assumed that the scouring extent and depth of the scouring pit reach a stable state under various conditions, and the scouring extent at the top of the scouring pit is equal to the bottom scouring extent ( $S_{tw} = S_w$ ). Only the soil and the lower five-bucket foundation of the FBjf are retained for the bearing capacity calculation to simplify the calculation. The five-bucket foundation is a rigid body, and the load application position is coupled at the middle of the top cover of the middle bucket. The heights of the bucket skirts are all 12 m, the  $D$  of the middle bucket is 26 m, and the  $D$  of the surrounding buckets is 18 m. The soil is modeled by a cylinder

300 m in diameter and 60 m in height, which is at least five times the maximum size of the five-bucket foundation in the corresponding directions to control the boundary effects for the calculation results [45].

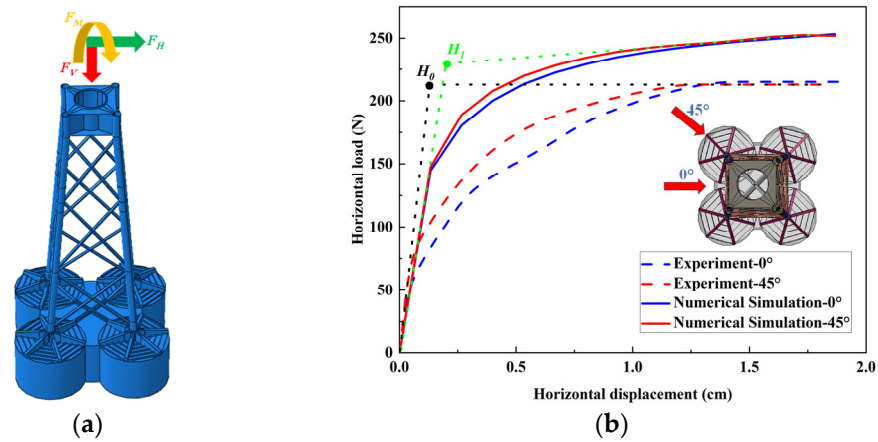


**Figure 6.** Numerical model verification: (a) Load direction; (b) Comparison of load–displacement curves.

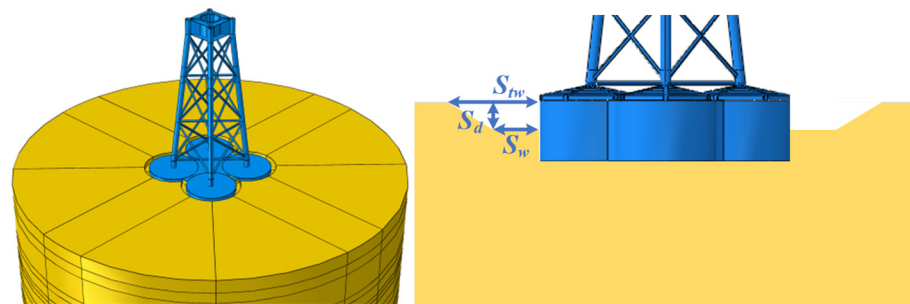


**Figure 7.** Schematic diagram of the scour pit.

During the numerical simulation process, the scouring depths are set at 2 m, 4 m, and 6 m, and the scouring extents are set at 2.7 m, 3.6 m, and 7.2 m, resulting in a total of nine orthogonal tests. Additionally, a reference condition without scouring is used for comparison. As described above, the ultimate bearing capacity of the FBJF is determined using the tangent method in the load–displacement curve. The intersection points of the two tangents for each condition in the load–displacement curve correspond to the displacement and load at which the FBJF reaches its ultimate bearing capacity. This method is used subsequently to determine the ultimate bearing capacity of the FBJF.

### 3.2. Results without Scouring

Based on the experimental and numerical simulation results in Section 3.1, it can be concluded that the horizontal bearing capacity of the FBJF under loading directions of 0° and 45° is almost the same. Therefore, the bearing capacity of the FBJF is calculated using the load direction of 0° in the following study. The load–displacement curve of the FBJF under monotonic loading without scouring is shown in Figure 8.

Under monotonic horizontal loading, the horizontal load increases rapidly as the horizontal displacement increases initially. After reaching a certain point, the horizontal load increases slowly with increasing horizontal displacement. It is determined by the tangent method that the  $H_{ult}$  of the FBJF under monotonic horizontal loading is 118 MN, with an ultimate horizontal displacement of 0.28 m. Under monotonic vertical loading, the  $V_{ult}$  of the FBJF is 3343 MN, with an ultimate vertical displacement of 6.4 m. Under monotonic bending loading, the  $M_{ult}$  of the FBJF is 1103 MN·m, with an ultimate angle of 0.012 rad.

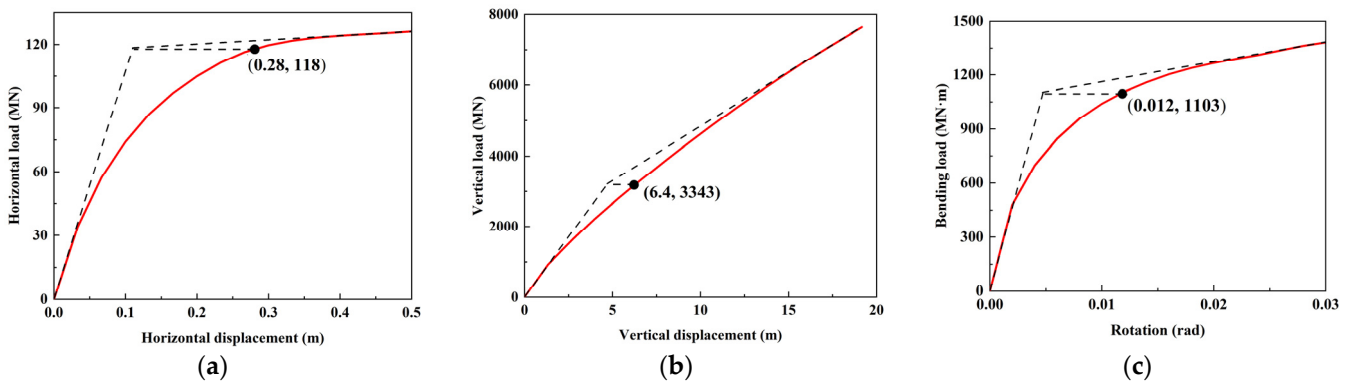


**Figure 8.** Bearing capacity curves under monotonic loading: (a) Horizontal load; (b) Vertical load; (c) Bending load.

Figure 9 shows the soil failure mechanism and PEEQ diagram of the FBJF under monotonic loading. Under monotonic  $F_H$ , the soil in the bucket sports horizontally together with the foundation due to the constraint of the FBJF. The soil behind the foundation collapses, forming an active failure zone. The soil in front is compressed to form a passive failure zone, and the plastic failure zone is relatively large to almost the entire height of the bucket skirt. Inside the FBJF, the soil on the front side is compressed to form a small passive failure area and is mainly concentrated near the tip of the bucket skirt. In addition, there is a rotating tendency under monotonic horizontal loading. The soil behind the FBJF is compressed through the bucket, and a small plastic failure area is formed near the tip of the bucket skirt.

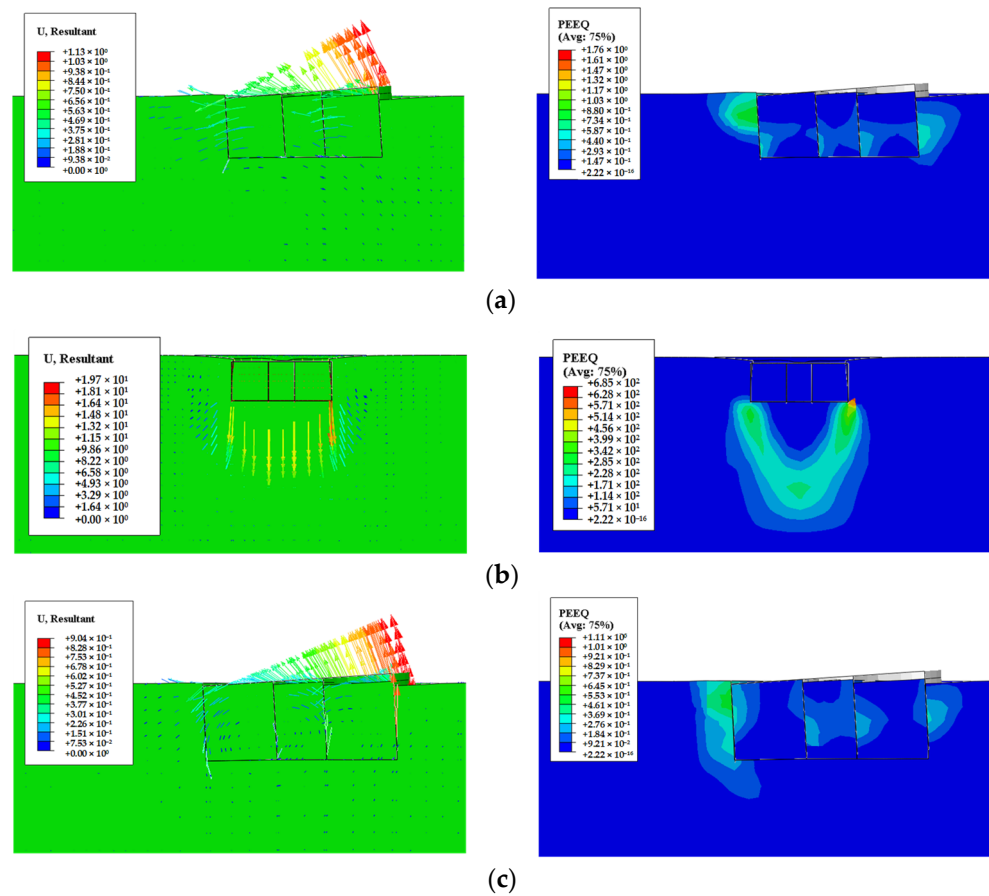


**Figure 9.** Vector and PEEQ diagrams: (a) Horizontal load; (b) Vertical load; (c) Bending load.

Under monotonic  $F_V$ , the soil in the bucket moves downwards together with the foundation due to the constraint of the FBJF, compressing the soil under the FBJF. The main failure happens near the tip of the skirt and extends downwards, forming a large failure area at the bottom of the foundation. Under monotonic  $F_M$ , the soil inside the buckets rotates around the centroid of the foundation due to the constraint of the FBJF. Similar to the soil failure mode under monotonic horizontal load, the soil behind the foundation collapses, forming an active failure zone. The soil in front is compressed to form a passive failure zone, and the plastic failure zone is relatively large: it is almost the entire height of the bucket skirt. Inside the FBJF, the soil on the front side is compressed to form a small passive failure area, and the failure area at the front position is mainly concentrated near the top cover of the bucket, while the plastic failure area at the back position is mainly concentrated near the middle of the bucket skirt. In addition, the soil behind the FBJF is compressed through the bucket due to the rotation, and a small plastic failure area is in the middle position of the bucket skirt.

### 3.3. Effect of Scouring Depth

In this section, the effects of the scouring depth on the bearing capacity of the FBJF under nine various scour conditions with a constant scouring extent are analyzed. In Figure 10, when the scouring extent is constant, the bearing capacity curves of the FBJF under monotonic  $F_H$  in different scour conditions are plotted, where  $S_w$  represents the scouring extent,  $S_d$  represents the scouring depth,  $D$  represents the bucket diameter of 18 m, and  $L$  represents the skirt height of 12 m. Under various scour conditions, the variation of the bearing capacity curve is similar. With the increase in horizontal displacement, the horizontal load increases rapidly at first and then increases slowly with displacement.

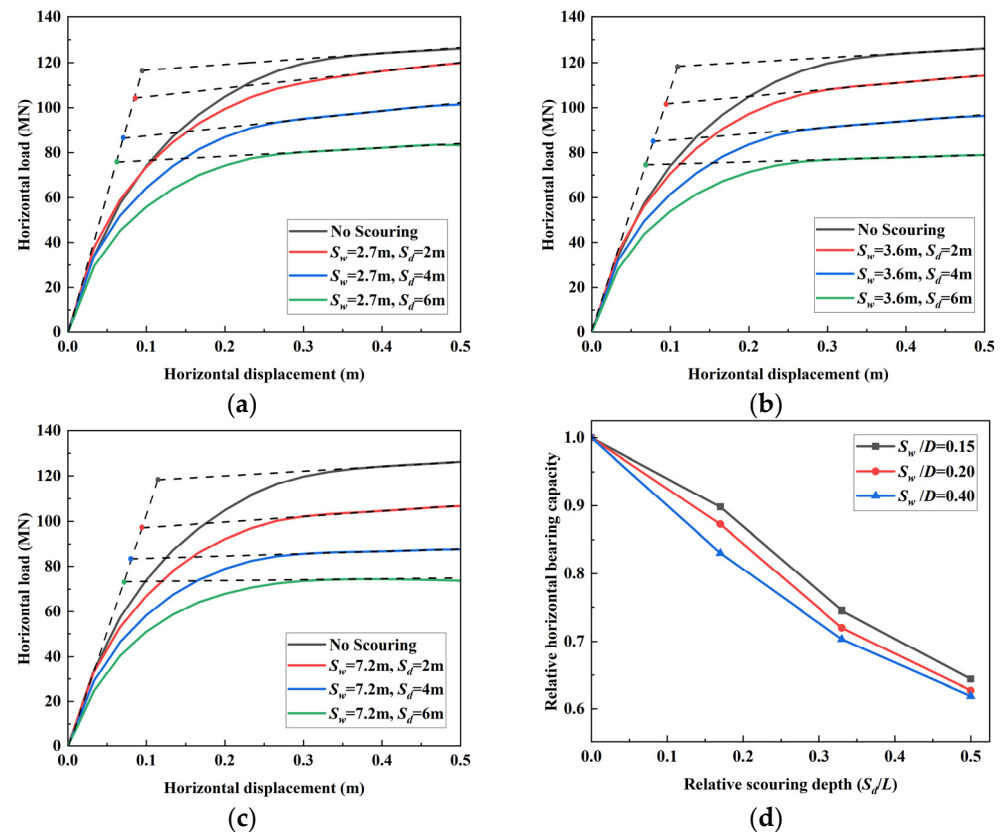


**Figure 10.** The  $H_{ult}$  at a constant scouring extent: (a)  $S_w = 2.7$  m; (b)  $S_w = 3.6$  m; (c)  $S_w = 7.2$  m; (d) Summarization.

When the scouring extent is 2.7 m, the  $H_{ult}$  of the FBJF is 106 MN and 76 MN for the scouring depths of 2 m and 6 m, respectively, which is reduced by about 10% and 36% compared to the  $H_{ult}$  of 118 MN without scouring. When the scouring extent is 3.6 m, the  $H_{ult}$  of the FBJF is 103 MN and 74 MN for the scouring depths of 2 m and 6 m, respectively, which is reduced by about 13% and 37% compared to the no-scour condition. When the scouring extent is 7.2 m, the  $H_{ult}$  of the FBJF is 98 MN and 73 MN for the scouring depths of 2 m and 6 m, respectively, which is reduced by about 17% and 38% compared to the no-scour condition. When the scouring extent is constant, the  $H_{ult}$  of the FBJF reduces linearly with the increasing scouring depth. It can be observed that the change in scouring depth affects the  $H_{ult}$  of the FBJF significantly. When the scouring depth is 2 m and 6 m, the maximum decline in the  $H_{ult}$  is 26% of the no-scour condition, and the minimum decline is 21%.

As shown in Figure 11, the  $M_{ult}$  of the FBJF under monotonic bending loading in different scour conditions is plotted when the scouring extent is constant. Under various scour conditions, the variation of the bending–rotation curve is similar. With increasing rotation angle, the bending load increases rapidly at first and then increases slowly with further rotation.

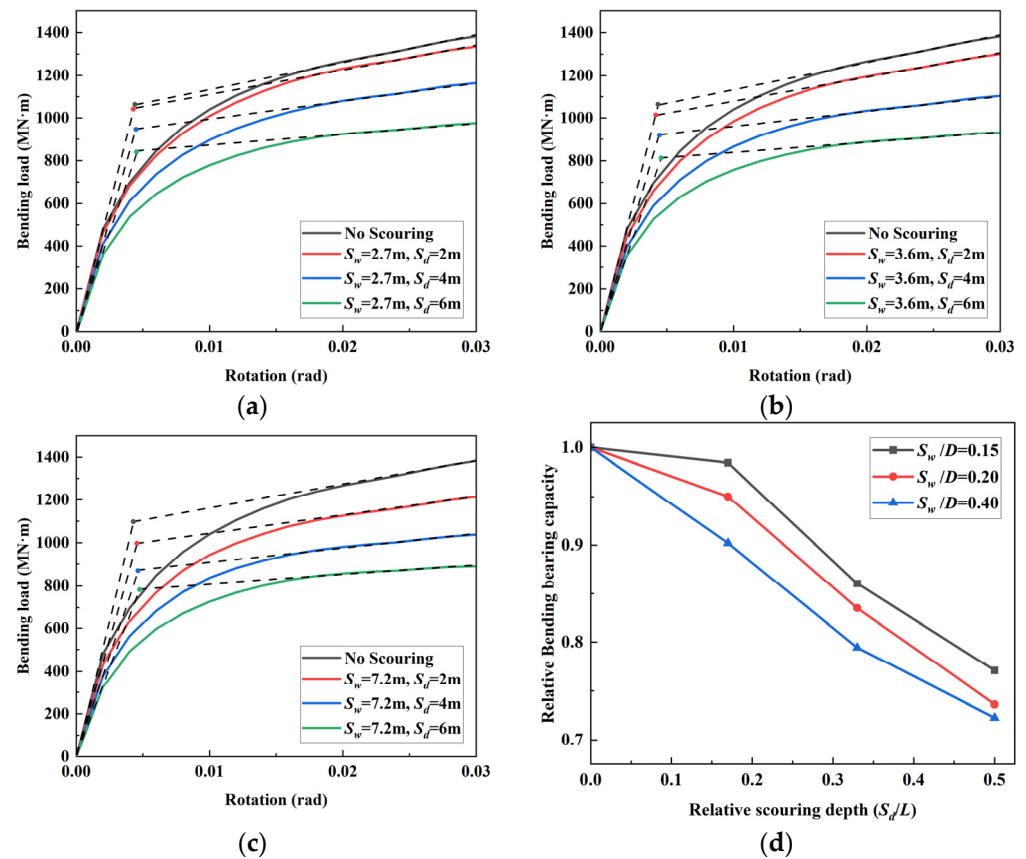


**Figure 11.** The  $M_{ult}$  at a constant scouring extent: (a)  $S_w = 2.7$  m; (b)  $S_w = 3.6$  m; (c)  $S_w = 7.2$  m; (d) Summarization.

When the scouring extent is 2.7 m, the  $M_{ult}$  of the FBJF is 1086 MN·m and 850 MN·m for the scouring depths of 2 m and 6 m, respectively, which is reduced by about 2% and 23% compared to the  $M_{ult}$  of 1103 MN·m without scouring. When the scouring extent is 3.6 m, the  $M_{ult}$  of the FBJF is 1048 MN·m and 812 MN·m for the scouring depths of 2 m and 6 m, respectively, which is reduced by about 5% and 26% compared to the no-scour condition. When the scouring extent is 7.2 m, the  $M_{ult}$  of the FBJF is 995 MN·m and 797 MN·m for the scouring depths of 2 m and 6 m, respectively, which is reduced by about 10% and 28% compared to the no-scour condition. When the scouring extent is constant, the  $M_{ult}$  of

the FBJF reduces linearly with the increasing scouring depth. It can be observed that the change in scouring depth affects the  $M_{ult}$  of the FBJF significantly. When the scouring depth is 2 m and 6 m, the maximum decline in the  $M_{ult}$  is 21% of the no-scour condition, and the minimum decline is 18%.

### 3.4. Effect of Scouring Extent

In this section, the impacts of the scouring extent on the bearing capacity of the FBJF at a constant scouring depth are analyzed. In Figure 12, when the scouring depth is constant, the load–displacement curves of the FBJF under monotonic horizontal load in different scour conditions are plotted. Under various scour conditions, the variation of the curve is similar. With increasing horizontal displacement, the horizontal load increases rapidly at first and then increases slowly with displacement.

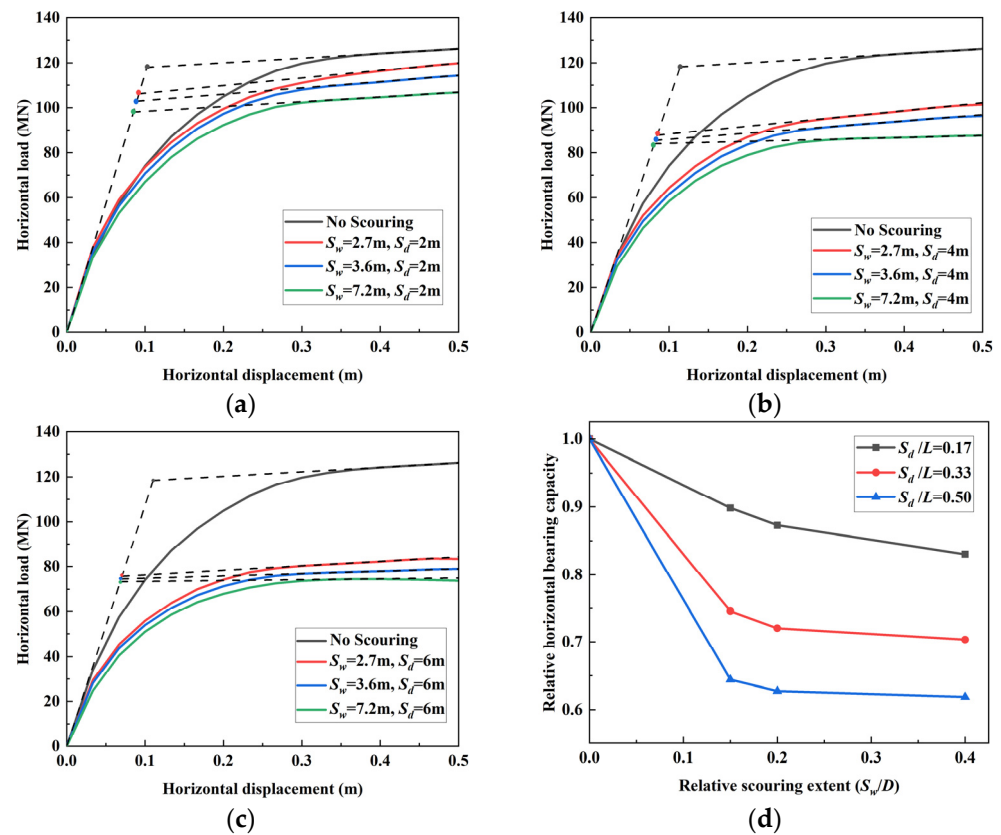


**Figure 12.** The  $H_{ult}$  at a constant scouring depth: (a)  $S_d = 2$  m; (b)  $S_d = 4$  m; (c)  $S_d = 6$  m; (d) Summarization.

When the scouring depth is 2 m, as the scouring extent changes from 2.7 m to 7.2 m, the  $H_{ult}$  of the FBJF decreases from 106 MN to 98 MN, which is reduced by about 10% and 17% compared to the  $H_{ult}$  of 118 MN without scouring. When the scouring depth is 4 m, as the scouring extent changes from 2.7 m to 7.2 m, the  $H_{ult}$  of the FBJF decreases from 88 MN to 83 MN, which is reduced by about 25% and 30% compared to the no-scour condition. When the scouring depth is 6 m, as the scouring extent changes from 2.7 m to 7.2 m, the  $H_{ult}$  of the FBJF decreases from 76 MN to 73 MN, which is reduced by about 36% and 38% compared to the no-scour condition. When the scouring depth is constant, the  $H_{ult}$  of the FBJF reduces slightly with the increasing scouring extent. It can be observed that the change in scouring extent affects the  $H_{ult}$  of the FBJF slightly. When the scouring extent changes from 2.7 m to 7.2 m, the maximum decline in the  $H_{ult}$  is 7% of the no-scour condition, and the minimum decline is 2%.

As shown in Figure 13, the bending–rotation curves of the FBJF under monotonic bending loading in different scour conditions are plotted when the scouring depth is constant. Under various scour conditions, the variation of the bending–rotation curve is similar. With the increase in rotation angle, the bending load increases rapidly at first and then increases slowly with further rotation.

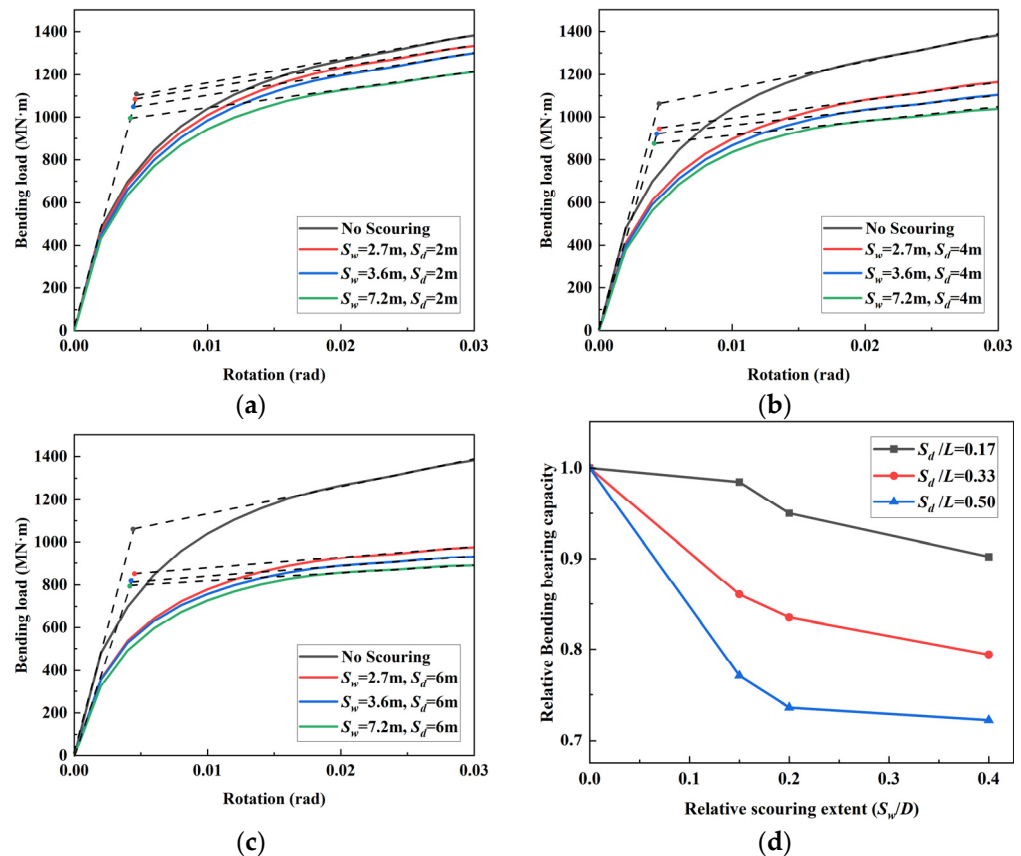


**Figure 13.** The  $M_{ult}$  at a constant scouring depth: (a)  $S_d = 2$  m; (b)  $S_d = 4$  m; (c)  $S_d = 6$  m; (d) Summarization.

When the scouring depth is 2 m, the  $M_{ult}$  of the FBJF is 1086 MN·m and 995 MN·m for the scouring extents of 2.7 m and 7.2 m, respectively, which is reduced by about 2% and 10% compared to the  $M_{ult}$  of 1103 MN·m without scouring. When the scouring depth is 4 m, the  $M_{ult}$  of the FBJF is 949 MN·m and 876 MN·m for the scouring depths of 2.7 m and 7.2 m, respectively, which is reduced by about 14% and 21% compared to the no-scour condition. When the scouring depth is 6 m, the  $M_{ult}$  of the FBJF is 850 MN·m and 797 MN·m for the scouring depths of 2.7 m and 7.2 m, respectively, which is reduced by about 23% and 28% compared to the no-scour condition. When the scouring depth is constant, the  $M_{ult}$  of the FBJF decreases slightly with the increasing scouring extent. It can be observed that the change in scouring depth affects the  $M_{ult}$  of the FBJF slightly. When the scouring extent changes from 2.7 m to 7.2 m, the maximum decline in the  $M_{ult}$  is 8% of the no-scour condition, and the minimum decline is 5%.

The variation rules for the bearing capacity of the FBJF after scouring are similar to the results of the WSBF and the MBFJF of Zhao et al. [40] and Li et al. [41]. The variation in scouring depth is more sensitive than that in scouring extent to the changes in bearing capacity. When the scouring depth is constant, the horizontal bearing capacity and moment bearing capacity of the FBJF change relatively little with the increase in scouring extent after the scouring extent exceeds 2.7 m.

Based on the above results, the bearing capacity of the FBJF is reduced under scouring. This is because the surrounding soil of the FBJF is hollowed out, losing the constraint of the

soil and part of the soil pressure. The interaction between the FBJF and the soil is reduced, leading to a decrease in bearing capacity. Moreover, an increase in scouring depth has a greater impact on the reduction of the bearing capacity of the FBJF than an increase in scouring extent. When the scouring extent increases to a certain extent, the bearing capacity of the FBJF does not change significantly with a further increase in scouring extent because the bearing capacity of the foundation is determined by the soil adjacent to the FBJF. The change of scouring depth must be the hollowing out of the soil adjacent to the FBJF, which leads to a significant reduction of the bearing capacity, so the factor of scouring depth should be paid attention to in the design of scour protection.

In addition, scouring can also damage the FBJF structure, and the increase in scouring depth has more influence on the damage of structure than the increase in scouring extent. Scouring causes the soil around the foundation to be hollowed out, and the bucket skirt of the FBJF is directly exposed to the marine environment. Due to the missing part of the constraint of the surrounding soil, the first-order natural frequency of the FBJF may change. If the overall OWT structure resonates, fatigue damage to the bucket skirt can occur, thus threatening the normal operation of the OWT. It is essential to consider that the fatigue damage experienced by the bucket skirt due to scouring is exacerbated by corrosion from the marine environment. This interaction between scouring and corrosion should be considered for a more comprehensive understanding of the structural challenges faced by the foundation.

#### 4. $F_H$ - $F_M$ Failure Envelope of the FBJF

##### 4.1. Methodology

There are mainly two methods to acquire the failure envelope of the FBJF, i.e., the swipe loading method and the fixed-displacement ratio method [29,46,47]. The swipe loading method requires high symmetry of the envelope and is relatively simple. Firstly, the load in a certain direction was applied to reach the bearing capacity in that direction, and then the load was applied in another direction to reach the bearing capacity. Thus, the approximate envelope profile can be determined in one step. The fixed-displacement ratio method adopts a displacement ratio in two directions as a loading path to obtain a point on the envelope for each loading path. Multiple points are obtained through various paths, and the corresponding envelope is obtained by fitting. This method does not require symmetry of the envelope and can search for the envelope under any loading combination. However, its calculation process is complex. Considering the dissymmetry of the  $F_H$ - $F_M$  envelope, this study adopted the second method to acquire the envelope. The fixed-displacement ratio ( $R = U_H/\theta$ ) was the ratio of horizontal displacement to the rotation angle, and a total of 14 values were considered, including  $-\infty$ ,  $-200$ ,  $-100$ ,  $-40$ ,  $-20$ ,  $-8$ ,  $0$ ,  $5$ ,  $8$ ,  $10$ ,  $12$ ,  $14$ ,  $16$ , and  $+\infty$ . Through these 14 paths, 14 points on the envelope were obtained. Subsequently, the  $F_H$ - $F_M$  failure envelope of the FBJF was determined by fitting. Furthermore, to determine a point in the envelope under the corresponding path, the  $F_H$  and  $F_M$  values correspond to the displacement and rotation values at the ultimate bearing capacity of the FBJF under monotonic loading.

##### 4.2. $F_H$ - $F_M$ Failure Envelope without Scouring

Figure 14 shows the  $F_H$ - $F_M$  failure envelope of the FBJF under combined loading without scouring. We can observe the asymmetry of the failure envelope of the FBJF in the first quadrant, and the horizontal load direction is consistent with the bending load direction, which is the most disadvantageous situation of the force in the design.

As the  $F_H$  increases, the  $M_{ult}$  of the FBJF decreases rapidly. In the second quadrant, the direction of  $F_H$  and  $F_M$  is opposite. As the  $F_H$  is small, a relatively small resisting bending load will occur, opposite to the applied bending load direction. As the horizontal load increases, the ultimate bending load gradually increases. When the ultimate moment load reaches its maximum value, it begins to decrease as the horizontal load continues to increase.

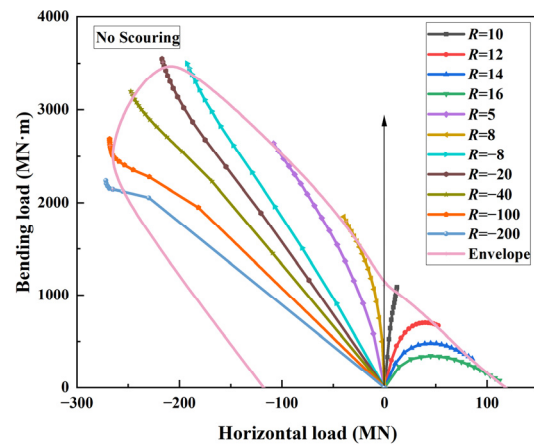


Figure 14.  $F_H-F_M$  failure envelope.

### 4.3. Effect of Scouring Depth on the $F_H-F_M$ Failure Envelope

For the effects of scouring depth on the  $F_H-F_M$  failure envelopes of the FBJF, taking the no-scour condition as the reference group, three different scour conditions were selected ( $S_w = 7.2$  m,  $S_d = 2$  m;  $S_w = 7.2$  m,  $S_d = 4$  m;  $S_w = 7.2$  m,  $S_d = 6$  m). Figure 15 shows that the  $F_H-F_M$  failure envelopes of the FBJF at various scouring depths are similar and show obvious asymmetry. The trend of the  $F_H-F_M$  failure envelope is consistent with that of the no-scour condition.

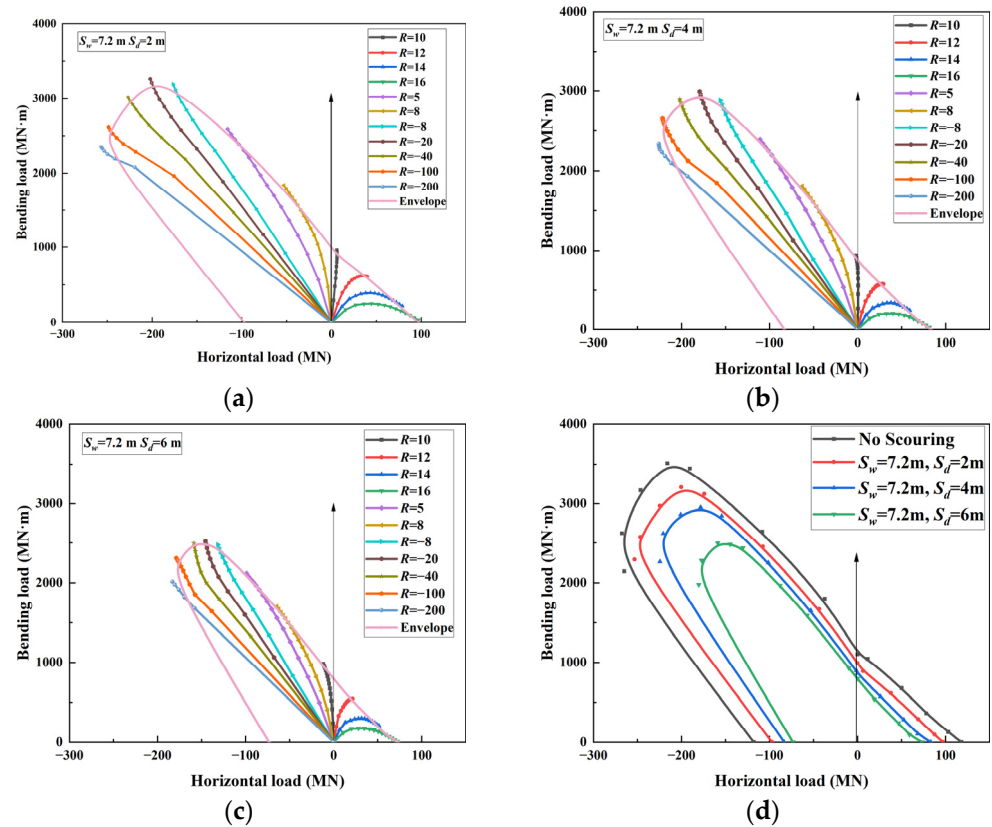


Figure 15.  $F_H-F_M$  failure envelope at a constant scouring extent: (a)  $S_w = 7.2$  m,  $S_d = 2$  m; (b)  $S_w = 7.2$  m,  $S_d = 4$  m; (c)  $S_w = 7.2$  m,  $S_d = 6$  m; (d) Summary.

With the increasing scouring depth, the profile of the envelope gradually contracts, which indicates that the  $H_{ult}$  and  $M_{ult}$  of the FBJF are both decreasing. In the first quadrant, the gaps between the envelopes of different scouring depths are relatively small at

this stage. In the second quadrant, when the horizontal load is small, the presence of a resisting bending load leads to an increase in the ultimate bending bearing capacity with an increase in horizontal load. At this stage, the gaps between the envelopes of different scouring depths are relatively small. However, after reaching the maximum value of the ultimate bending bearing capacity, with an increase in horizontal load, the gaps between the envelopes of different scouring depths in this stage are relatively large. Therefore, the variation in scouring depth has a greater effect on the envelopes in this stage than in the first two stages.

4.4. Effect of Scouring Extent on the  $F_H$ - $F_M$  Failure Envelope

For the effects of scouring extent on the  $F_H$ - $F_M$  failure envelopes of the FBGF, taking the no-scour condition as the reference group, three different scour conditions were selected ( $S_w = 2.7$  m,  $S_d = 6$  m;  $S_w = 3.6$  m,  $S_d = 6$  m;  $S_w = 7.2$  m,  $S_d = 6$  m). Figure 16 shows that the  $F_H$ - $F_M$  failure envelopes of the FBGF at different scouring extents are very similar and show obvious asymmetry. The variation trend of the  $F_H$ - $F_M$  failure envelope is consistent with that of the no-scour condition.

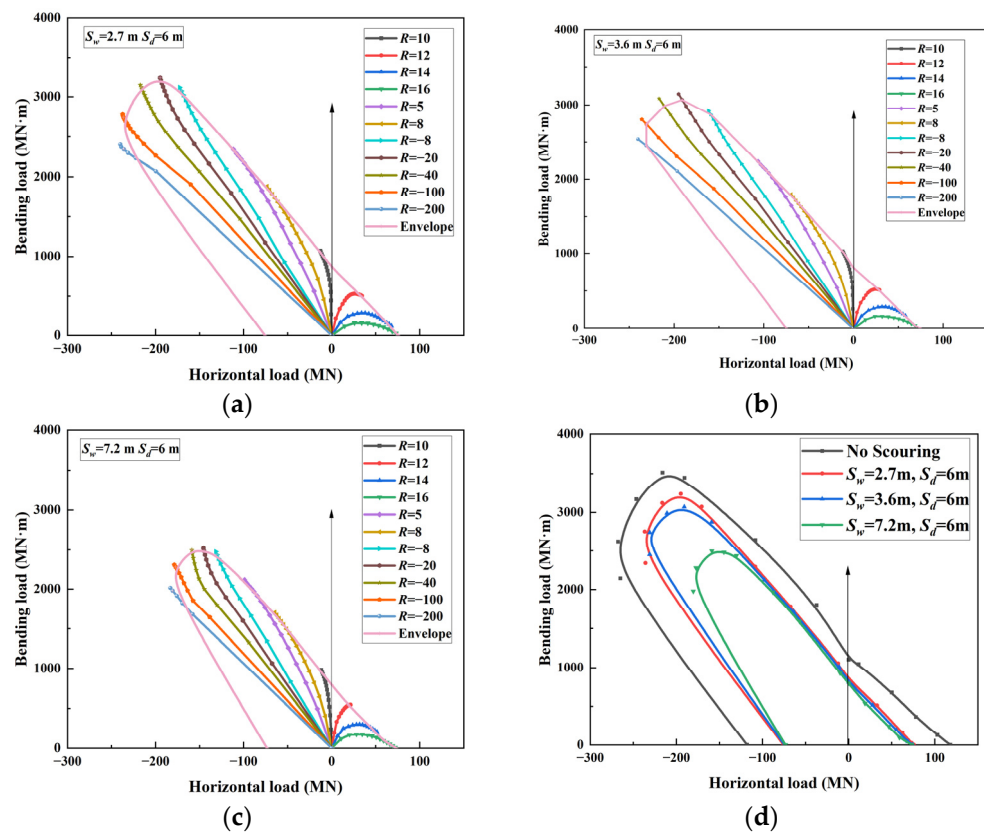


Figure 16.  $F_H$ - $F_M$  failure envelope at a constant scouring depth: (a)  $S_w = 2.7$  m,  $S_d = 6$  m; (b)  $S_w = 3.6$  m,  $S_d = 6$  m; (c)  $S_w = 7.2$  m,  $S_d = 6$  m; (d) Summary.

With the increasing scouring extent, the profile of the envelope gradually contracts, which indicates that the  $H_{ult}$  and  $M_{ult}$  of the FBGF are both decreasing. In the first quadrant, the gaps between the envelopes of different scouring depths are relatively small at this stage. In the second quadrant, when the  $F_H$  is small, the presence of a resisting bending load leads to an increase in the ultimate bending bearing capacity with the increasing horizontal load. At this stage, the envelopes of different scouring extents are almost overlapping, indicating that the scouring extent currently is no longer a determining factor for the bearing capacity of the FBGF. However, after reaching the maximum value of the  $M_{ult}$ , with increasing horizontal load, the gaps between the envelopes of different scouring extents in this stage are relatively large.

The variation rules for the  $F_H-F_M$  failure envelopes of the FBjF after scouring are similar to the results of the WSBF and the MBjF of Zhao et al. [40] and Li et al. [41]. Comparatively, the variations of the  $F_H-F_M$  failure envelope are more sensitive to changes in scouring depth than scouring extent. When the scouring extent is constant, the  $F_H-F_M$  failure envelope of the FBjF gradually contracts inward with the increasing scouring depth, showing significant variation. However, when the scouring depth is constant, and after the scouring extent exceeds 2.7 m, the variation in the  $F_H-F_M$  failure envelope of the FBjF is relatively small with the increasing scouring extent.

### 5. $F_V-F_H-F_M$ Failure Envelope of the FBjF

#### 5.1. $F_V-F_H-F_M$ Failure Envelope without Scouring

To investigate the  $F_V-F_H-F_M$  failure envelope of the FBjF under vertical, horizontal, and bending load combinations,  $F_V$  was set as  $0 V_{ult}$ ,  $0.25 V_{ult}$ ,  $0.5 V_{ult}$ , and  $0.75 V_{ult}$ , where  $V_{ult}$  is the vertical bearing capacity of the FBjF under each condition. The  $V_{ult}$  of the FBjF is 3343 MN without scouring, and the fixed-displacement method described in Section 4.2 is utilized. As shown in Figure 17, the profile of the envelope changes significantly with the  $F_V$ . As the  $F_V$  increases, the profile of the envelope first extends outward and then contracts inward. When the  $F_V$  is  $0.25 V_{ult}$ , the profile of the envelope is the largest, indicating the maximum bearing capacity of the FBjF. When the  $F_V$  continues to increase, the profile of the envelope contracts inward, resulting in a decreasing bearing capacity.

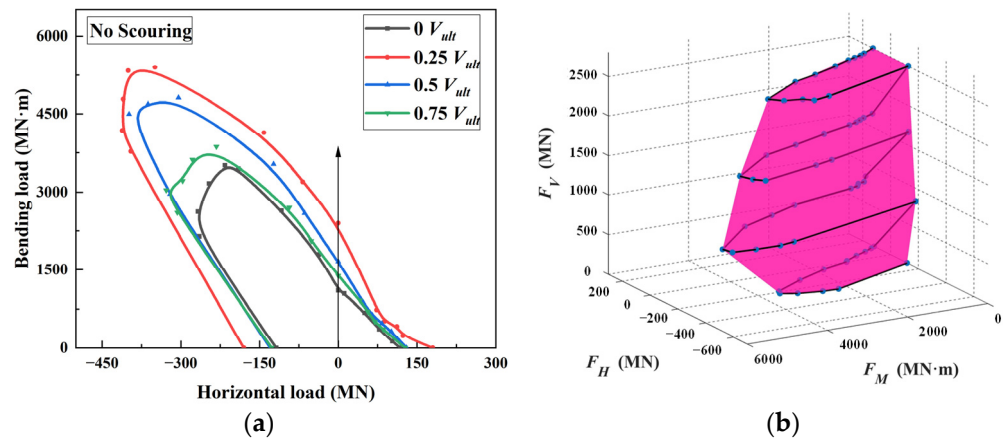


**Figure 17.**  $F_V-F_H-F_M$  three-dimensional failure envelope without scouring: (a)  $F_H-F_M$  failure envelope; (b) Three-dimensional failure envelope.

According to the  $F_H-F_M$  failure envelopes under various  $F_V$  of the FBjF, the  $F_V-F_H-F_M$  failure envelope of the FBjF under no-scour condition was obtained using interpolation methods in MATLAB R2019a, as shown in Figure 17. It is observed that with the increasing  $F_V$ , the three-dimensional failure envelope first extends outward and then contracts inward, and the whole three-dimensional envelope is a closed ellipsoid.

#### 5.2. Effect of Scouring Degree

For the effects of scouring on the  $F_V-F_H-F_M$  failure envelope of the FBjF, three different scour conditions were selected ( $S_w = 2.7$  m,  $S_d = 6$  m;  $S_w = 7.2$  m,  $S_d = 2$  m;  $S_w = 7.2$  m,  $S_d = 6$  m), and the  $V_{ult}$  of the FBjF were 2480 MN, 2333 MN and 2307 MN, respectively. Figure 18 shows the  $F_V-F_H-F_M$  failure envelopes of the FBjF under three different scour conditions. Under different scour conditions, the  $F_V-F_H-F_M$  failure envelope profiles of the FBjF are similar, and the variation trend is consistent with the no-scour condition.

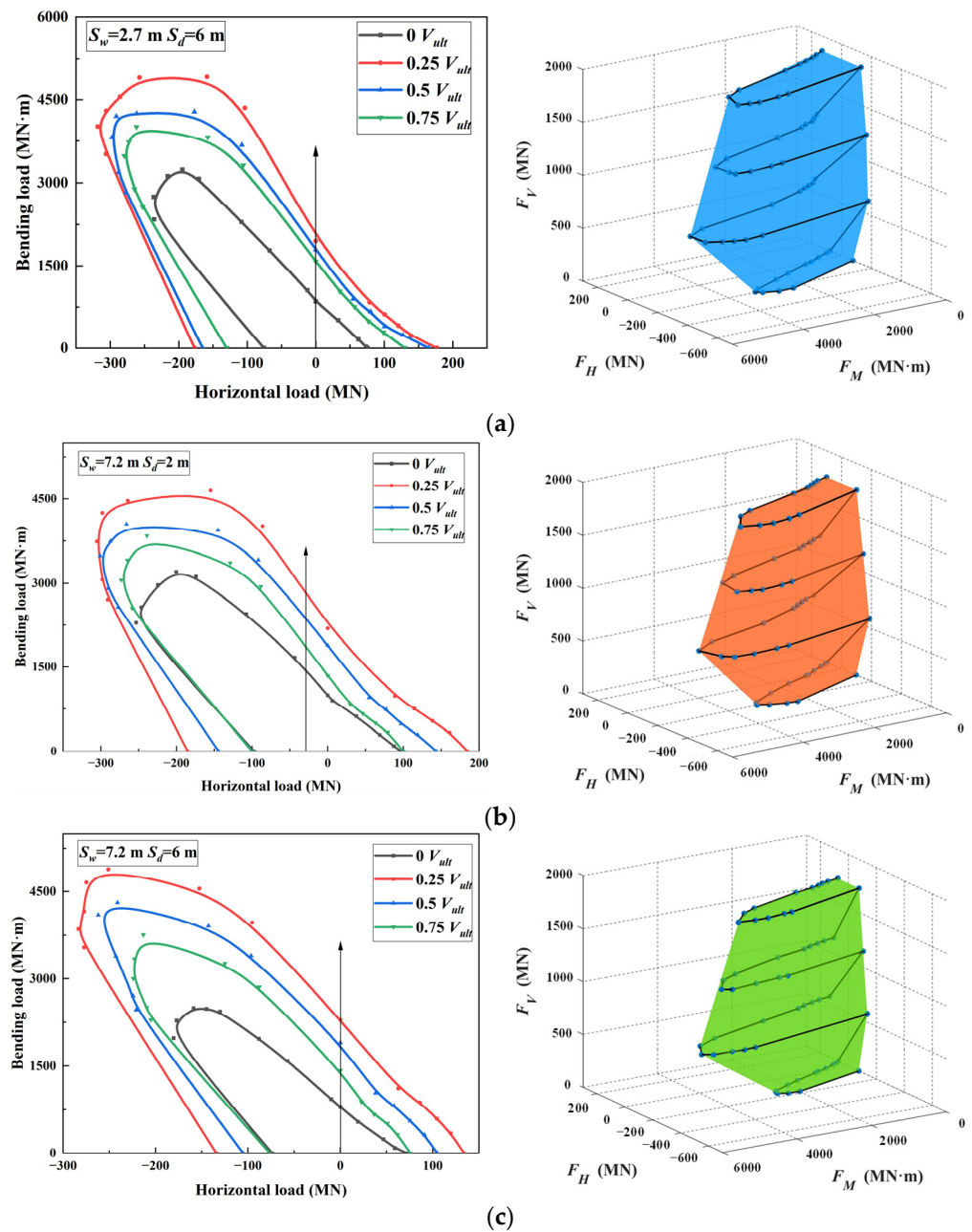


**Figure 18.**  $F_V$ - $F_H$ - $F_M$  three-dimensional failure envelope under scouring: (a)  $S_w = 2.7$  m,  $S_d = 6$  m; (b)  $S_w = 7.2$  m,  $S_d = 2$  m; (c)  $S_w = 7.2$  m,  $S_d = 6$  m.

The whole three-dimensional envelope is a closed ellipsoid. As the vertical load increases, the three-dimensional failure envelope gradually protrudes first and then gradually contracts. When the vertical load is  $0.25 V_{ult}$ , the envelope protrudes the most, indicating the bearing capacity of the FBJF is maximum. As the vertical load continues to increase, the envelope contracts inward, and the bearing capacity decreases. Therefore, when the surrounding soil of the FBJF is subject to scouring, it is advisable to increase the vertical load appropriately within the range of  $0.25 V_{ult}$  and thus improve the bearing capacity of the FBJF to ensure safe operation. However, other measures are also necessary to prevent scouring, such as optimizing the location of offshore wind turbine foundations, using specific construction methods, applying anti-scouring coatings on foundation surfaces, or throwing stones around the foundation after installation.

The variation rules for the  $F_V$ - $F_H$ - $F_M$  failure envelopes of the FBJF after scouring are similar to the results of the WSBF and the MBJF by Zhao et al. [40] and Li et al. [41]. With

the increasing vertical load, the  $F_V$ - $F_H$ - $F_M$  failure envelope protrudes outward and then shrinks inward. The  $F_V$ - $F_H$ - $F_M$  failure envelope profiles of the same foundation under different scouring conditions are identical. In addition, for the FBJF and the WSBF, the most prominent three-dimensional envelope surface is at a vertical load of  $0.25 V_{ult}$ , whereas that of the MBJF is at a vertical load of  $0.5 V_{ult}$ .

## 6. Conclusions

In this study, a novel FBJF was proposed based on the trends of deep-sea and large-capacity OWT foundations. Then, a series of local-scour simplified finite-element models were established using ABAQUS. The effects of scouring depth and extent on the ultimate bearing capacity of the FBJF were also analyzed and quantified. Furthermore, based on the fixed-displacement ratio method, the failure envelopes of the FBJF were obtained, and the effects of various scour conditions on the failure envelopes were compared. The main conclusions obtained are as follows:

(1) When the scouring extent is constant, the  $H_{ult}$  and  $M_{ult}$  of the FBJF decline with the increasing scouring depth. The maximum reduction in the horizontal bearing capacity of the no-scour condition is 26%, and the maximum reduction in the bending bearing capacity of the no-scour condition is 21%. When the scouring depth is constant, the  $H_{ult}$  and  $M_{ult}$  of the FBJF decline with the increasing scouring extent. The maximum decrease in  $H_{ult}$  is 7% in the no-scour condition, and the maximum decrease in  $M_{ult}$  is 8% in the no-scour condition. Compared with the scouring extent, the change in scouring depth has a more significant effect on the bearing capacity of the FBJF. At a maximum scouring depths of 6 m, the  $H_{ult}$  and  $M_{ult}$  are 62% and 72% in the no-scour condition, respectively.

(2) Under different scour conditions, the  $F_H$ - $F_M$  failure envelopes of the FBJF under the combined loading mode have similar profiles and variation trends and show obvious asymmetry. With the increasing scouring depth, the profile of the envelope contracts inward gradually, and the  $H_{ult}$  and  $M_{ult}$  of the FBJF decrease. As the scouring extent increases, the profile of the envelope contracts inward gradually, and after the scour extent exceeds 2.7 m, the envelopes located in the first quadrant are almost overlapping, indicating that the change in scouring extent currently is not a key factor for the bearing capacity of the FBJF.

(3) Based on the calculation of failure envelopes of the FBJF under various  $F_V$ , the  $F_V$ - $F_H$ - $F_M$  failure envelopes of the FBJF under various scour conditions are obtained using the interpolation method. The  $F_V$ - $F_H$ - $F_M$  failure envelopes under various scour conditions are similar, and the whole three-dimensional envelope is a closed ellipsoid. With the  $F_V$  increases, the three-dimensional failure envelope firstly gradually protrudes outward and then contracts inward. When the vertical load is  $0.25 V_{ult}$ , the envelope is the most convex, and the bearing capacity of the FBJF reaches the maximum. When the vertical load continues to increase, the envelope contracts inward, and the bearing capacity of the FBJF gradually reduces. This is because when the vertical load is within the range of  $0.25 V_{ult}$ , the soil pressure of the soil inside the bucket increases, and the lateral friction resistance of the bucket becomes larger, which enhances the bearing capacity of the FBJF. However, when the vertical load exceeds  $0.25 V_{ult}$ , the bucket and the soil will undergo a relative slide, which will lead to the reduction of the bearing capacity.

In this study, a simplified scour model of the FBJF was established using ABAQUS, and the effects of scouring on the bearing capacity of the FBJF were analyzed, which had some limitations. In the future, a more detailed scour model of the FBJF could be developed by carrying out an in-depth study. The effects of scouring on the torsional capacity of the FBJF can be investigated with the consideration of vertical capacity, horizontal capacity, and bending capacity. Furthermore, the effects of scouring on the structural damage of the foundation need further investigation. Finally, methods to optimize the structure to reduce the effects of scouring and scouring protection measures are also to be studied.

**Author Contributions:** Conceptualization, J.L., H.W., Y.G. and H.Z.; Methodology, J.L., H.W., Y.G. and H.Z.; Software, H.Z.; Validation, H.Z.; Formal analysis, H.Z.; Resources, J.L.; Data curation, H.Z.; Writing—original draft, H.Z.; Writing—review and editing, H.Z.; Supervision, J.L., H.W. and Y.G.; Project administration, J.L. All authors have read and agreed to the published version of the manuscript.

**Funding:** This research received no external funding.

**Data Availability Statement:** Data are contained within the article.

**Conflicts of Interest:** The authors declare no conflicts of interest.

## Nomenclature

### Variables

$D$	Diameter of the bucket
$L$	Length of the bucket skirt
$R$	Fixed-displacement ratio
$U_H$	Horizontal displacement
$\theta$	Rotation angle
$F_H$	Horizontal load
$F_V$	Vertical load
$F_M$	Bending load
$S_d$	Scouring depth
$S_w$	Bottom width of scouring extent
$S_{tw}$	Top width of scouring extent
$H_0$	Experimental horizontal bearing capacity
$H_1$	Numerical horizontal bearing capacity
$V_{ult}$	Ultimate vertical bearing capacity
$H_{ult}$	Ultimate horizontal bearing capacity
$M_{ult}$	Ultimate bending bearing capacity

### Abbreviations

OWT	Offshore wind turbine
FBJF	Five-bucket jacket foundation
WSBF	Wide-shallow bucket foundation
MBJF	Multi-bucket jacket foundation
PEEQ	Equivalent plastic strain

## References

- Leung, D.Y.; Yang, Y. Wind energy development and its environmental impact: A review. *Renew. Sustain. Energy Rev.* **2012**, *16*, 1031–1039. [[CrossRef](#)]
- Koh, J.; Ng, E. Downwind offshore wind turbines: Opportunities, trends and technical challenges. *Renew. Sustain. Energy Rev.* **2016**, *54*, 797–808. [[CrossRef](#)]
- de Azevedo, H.D.M.; Araújo, A.M.; Bouchonneau, N. A review of wind turbine bearing condition monitoring: State of the art and challenges. *Renew. Sustain. Energy Rev.* **2016**, *56*, 368–379. [[CrossRef](#)]
- Keivanpour, S.; Ramudhin, A.; Kadi, D.A. The sustainable worldwide offshore wind energy potential: A systematic review. *J. Renew. Sustain. Energy* **2017**, *9*, 065902. [[CrossRef](#)]
- Sahu, B.K. Wind energy developments and policies in China: A short review. *Renew. Sustain. Energy Rev.* **2018**, *81*, 1393–1405. [[CrossRef](#)]
- Guo, Y.; Wang, H.; Lian, J. Review of integrated installation technologies for offshore wind turbines: Current progress and future development trends. *Energy Convers. Manag.* **2022**, *255*, 115319. [[CrossRef](#)]
- Ding, H.-Y.; Feng, Z.-T.; Zhang, P.-Y.; Le, C.-H. Integrated Towing Transportation Technique for Offshore Wind Turbine with Composite Bucket Foundation. *China Ocean Eng.* **2022**, *36*, 133–143. [[CrossRef](#)]
- Bhattacharya, S. Challenges in Design of Foundations for Offshore Wind Turbines. *Eng. Technol. Ref.* **2014**, *1*, 922. [[CrossRef](#)]
- Li, Y.; Ong, M.C.; Tang, T. Numerical analysis of wave-induced poro-elastic seabed response around a hexagonal gravity-based offshore foundation. *Coast. Eng.* **2018**, *136*, 81–95. [[CrossRef](#)]
- Jiang, J.; Lian, J.; Dong, X.; Wang, H.; Zhou, H. Soil damping calculation of the offshore wind turbine supported by wide-shallow bucket foundation. *Appl. Ocean Res.* **2021**, *111*, 102682. [[CrossRef](#)]
- Lin, Z.; Pokrajac, D.; Guo, Y.; Jeng, D.-S.; Tang, T.; Rey, N.; Zheng, J.; Zhang, J. Investigation of nonlinear wave-induced seabed response around mono-pile foundation. *Coast. Eng.* **2017**, *121*, 197–211. [[CrossRef](#)]

12. Zhang, P.; Li, J.; Gan, Y.; Zhang, J.; Qi, X.; Le, C.; Ding, H. Bearing capacity and load transfer of brace topological in offshore wind turbine jacket structure. *Ocean Eng.* **2020**, *199*, 107037. [[CrossRef](#)]
13. Li, J.; Hu, G.; Jin, G.; Sun, Z.; Zong, Z.; Jiang, Y. Hydrodynamic Performance of a Novel Floating Foundation for an Offshore Wind Turbine Under a Storm Condition. *Int. J. Offshore Polar Eng.* **2020**, *30*, 120–128. [[CrossRef](#)]
14. Shi, W.; Zhang, L.; Karimirad, M.; Michailides, C.; Jiang, Z.; Li, X. Combined effects of aerodynamic and second-order hydrodynamic loads for floating wind turbines at different water depths. *Appl. Ocean Res.* **2023**, *130*, 103416. [[CrossRef](#)]
15. Ding, H.; Peng, Y.; Zhang, P.; Zhai, H.; Jia, N. Model Tests on the Penetration Resistance of Bucket Foundations for Offshore Wind Turbines in Sand. *J. Mar. Sci. Eng.* **2020**, *8*, 368. [[CrossRef](#)]
16. Natarajan, A.; Stolpe, M.; Wandji, W.N. Structural optimization based design of jacket type sub-structures for 10 MW offshore wind turbines. *Ocean Eng.* **2019**, *172*, 629–640. [[CrossRef](#)]
17. Liu, X.-Q.; Le, C.-H.; Zhao, M.-J.; Ding, H.-Y.; Zhang, P.; Lv, N.; Luo, S. Experimental Study on Influencing Factors of Motion Responses for Air-Floating Tetrapod Bucket Foundation. *China Ocean Eng.* **2022**, *36*, 258–267. [[CrossRef](#)]
18. Wang, L.; Zhou, W.; Guo, Z.; Rui, S. Frequency change and accumulated inclination of offshore wind turbine jacket structure with piles in sand under cyclic loadings. *Ocean Eng.* **2020**, *217*, 108045. [[CrossRef](#)]
19. Haver, S. A possible freak wave event measured at the draupner jacket january 1 1995. In Proceedings of the Rogue Waves of the Conference, Brest, France, 20–22 October 2004.
20. Bye, A.; Erbrich, C.; Rognlien, B.; Tjelta, T. Geotechnical design of bucket foundations. In Proceedings of the Offshore Technology of the Conference, Houston, TX, USA, 1–4 May 1995.
21. Ehrmann, A.; Penner, N. Offshore support structures with suction buckets: Parameter fitting of a simplified foundation model. In Proceedings of the International Ocean and Polar Engineering of the Conference, Rhodes, Greece, 26 June 2016.
22. Shen, K.; Zhang, Y.; Klinkvort, R.; Sturm, H.; Jostad, H.; Sivasithamparam, N.; Guo, Z. Numerical simulation of suction bucket under vertical tension loading. In Proceedings of the 8th International Conference on Offshore Site Investigation and Geotechnics, London, UK, 14 September 2017.
23. Dekker, M. Achievement under pressure: Suction pile jackets for the aberdeen offshore wind farm. In Proceedings of the WindEurope 2018 Conference, Hamburg, Germany, 25–28 September 2018.
24. Zhang, P.; He, S.; Liu, Y.; Ding, H. Force transfer characteristics of composite bucket foundation for offshore wind turbines. *J. Renew. Sustain. Energy* **2016**, *8*, 013307. [[CrossRef](#)]
25. Hentati, A.; Selmi, M.; Kormi, T.; Ali, N.B.H. Probabilistic HM failure envelopes of strip foundations on spatially variable soil. *Comput. Geotech.* **2018**, *102*, 66–78. [[CrossRef](#)]
26. Ding, H.; Liu, Y.; Zhang, P.; Le, C. Model tests on the bearing capacity of wide-shallow composite bucket foundations for offshore wind turbines in clay. *Ocean Eng.* **2015**, *103*, 114–122. [[CrossRef](#)]
27. Liu, M.; Lian, J.; Yang, M. Experimental and numerical studies on lateral bearing capacity of bucket foundation in saturated sand. *Ocean Eng.* **2017**, *144*, 14–20. [[CrossRef](#)]
28. Jia, N.; Zhang, P.; Liu, Y.; Ding, H. Bearing capacity of composite bucket foundations for offshore wind turbines in silty sand. *Ocean Eng.* **2018**, *151*, 1–11. [[CrossRef](#)]
29. Wang, J.; Liu, R.; Yang, X.; Chen, G. An optimised failure envelope approach of bucket foundation in undrained clay. *Ships Offshore Struct.* **2021**, *16*, 42–55. [[CrossRef](#)]
30. Yin, S. Undrained failure envelope for skirted spudcan foundations in clay under combined loading. *Mar. Georesources Geotechnol.* **2022**, *40*, 181–203. [[CrossRef](#)]
31. Gourvenec, S.; Steinepreis, M. Undrained Limit States of Shallow Foundations Acting in Consort. *Int. J. Géoméch.* **2007**, *7*, 194–205. [[CrossRef](#)]
32. Gourvenec, S.; Jensen, K. Effect of Embedment and Spacing of Cojoined Skirted Foundation Systems on Undrained Limit States under General Loading. *Int. J. Géoméch.* **2009**, *9*, 267–279. [[CrossRef](#)]
33. Kim, S.-R.; Hung, L.C.; Oh, M. Group effect on bearing capacities of tripod bucket foundations in undrained clay. *Ocean Eng.* **2014**, *79*, 1–9. [[CrossRef](#)]
34. Hung, L.C.; Kim, S.-R. Evaluation of combined horizontal-moment bearing capacities of tripod bucket foundations in undrained clay. *Ocean Eng.* **2014**, *85*, 100–109. [[CrossRef](#)]
35. Tran, N.X.; Hung, L.C.; Kim, S.-R. Evaluation of horizontal and moment bearing capacities of tripod bucket foundations in sand. *Ocean Eng.* **2017**, *140*, 209–221. [[CrossRef](#)]
36. Yu, T.; Lian, J.; Shi, Z.; Wang, H. Experimental investigation of current-induced local scour around composite bucket foundation in silty sand. *Ocean Eng.* **2016**, *117*, 311–320. [[CrossRef](#)]
37. Liang, S.; Zhang, Y.; Yang, J. An experimental study on pile scour mitigating measures under waves and currents. *Sci. China Technol. Sci.* **2015**, *58*, 1031–1045. [[CrossRef](#)]
38. Kishore, Y.N.; Rao, S.N.; Mani, J.S. The behavior of laterally loaded piles subjected to scour in marine environment. *KSCE J. Civ. Eng.* **2009**, *13*, 403–408. [[CrossRef](#)]
39. Ni, S.-H.; Huang, Y.-H.; Lo, K.-F. Numerical Investigation of the Scouring Effect on the Lateral Response of Piles in Sand. *J. Perform. Constr. Facil.* **2012**, *26*, 320–325. [[CrossRef](#)]
40. Zhao, X.; Zhang, P.; Lv, Y.; Ding, H. Scour effects on bearing capacity of composite bucket foundation for offshore wind turbines. *Mar. Georesources Geotechnol.* **2020**, *38*, 223–237. [[CrossRef](#)]

41. Li, J.; Guo, Y.; Lian, J.; Wang, H. Scour effects on the bearing capacity of multi-bucket jacket foundation for offshore wind turbines. *Ocean Eng.* **2022**, *259*, 111848. [[CrossRef](#)]
42. Mansur, C.I.; Kaufman, R.I. Pile tests, low-sill structure, old river, louisiana. *Trans. Am. Soc. Civ. Eng.* **1958**, *123*, 715–743. [[CrossRef](#)]
43. Jara, F.A.V. Model Testing of Foundations for Offshore Wind Turbines. Ph.D. Thesis, Oxford University, Oxford, UK, 2006.
44. Zhu, B.; Wen, K.; Kong, D.Q.; Zhu, Z.J.; Wang, L.J. A numerical study on the lateral loading behaviour of offshore tetrapod piled jacket foundations in clay. *Appl. Ocean. Res.* **2018**, *75*, 165–177. [[CrossRef](#)]
45. Selmi, M.; Kormi, T.; Hentati, A.; Ali, N.B.H. Capacity assessment of offshore skirted foundations under HM combined loading using RFEM. *Comput. Geotech.* **2019**, *114*, 103148. [[CrossRef](#)]
46. Tan, F. Centrifuge and Theoretical Modelling of Conical Footings on Sand. Ph.D. Thesis, University of Cambridge, Cambridge, UK, 1990.
47. Liu, R.; Wang, L.; Ding, H.Y.; Lian, J.J.; Li, B.R. Failure envelopes of large-diameter shallow buried bucket foundation in undrained saturated soft clay under combined loading conditions. *Chin. J. Geotech. Eng.* **2014**, *36*, 146–154.

**Disclaimer/Publisher’s Note:** The statements, opinions and data contained in all publications are solely those of the individual author(s) and contributor(s) and not of MDPI and/or the editor(s). MDPI and/or the editor(s) disclaim responsibility for any injury to people or property resulting from any ideas, methods, instructions or products referred to in the content.